Photoinduced Charge Transfer Dynamics in the Carotenoid−Porphyrin−C$_{60}$ Triad via the Linearized Semiclassical Nonequilibrium Fermi's Golden Rule

Zhubin Hu, Zhengqing Tong, Margaret S. Cheung, Barry D. Dunietz, Eitan Geva, and Xiang Sun*

ACCESS | 📊 Metrics & More | 📰 Article Recommendations | 🆂🅸 Supporting Information

ABSTRACT: The nonequilibrium Fermi's golden rule (NE-FGR) describes the time-dependent rate coefficient for electronic transitions when the nuclear degrees of freedom start out in a nonequilibrium state. In this paper, the linearized semiclassical (LSC) approximation of the NE-FGR is used to calculate the photoinduced charge transfer (CT) rates in the carotenoid−porphyrin−C$_{60}$ molecular triad dissolved in explicit tetrahydrofuran. The initial nonequilibrium state corresponds to impulsive photoexcitation from the equilibrated ground state to the $\pi\pi^*$ state, and the porphyrin-to-C$_{60}$ and carotenoid-to-C$_{60}$ CT rates are calculated. Our results show that accounting for the nonequilibrium nature of the initial state significantly enhances the transition rate of the porphyrin-to-C$_{60}$ CT process. We also derive the instantaneous Marcus theory (IMT) from LSC NE-FGR, which casts the CT rate coefficients in terms of a Marcus-like expression, with explicitly time-dependent reorganization energy and reaction free energy. IMT is found to reproduce the CT rates in the system under consideration remarkably well.
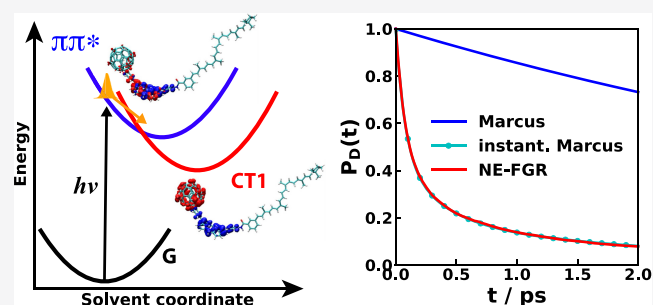
1. INTRODUCTION

Photoinduced charge transfer (CT) processes have been the subject of intensive research efforts over the last several decades due to their fundamental importance in cellular respiration,[1] repair of photodamaged DNA,[2] photosynthesis,[3,4] photocatalysis,[5] and organic photovoltaics (OPV).[6−18] A variety of first-principle computational methods for calculating photoinduced CT rates have been proposed for and applied to gas-phase molecules.[19−23] However, the development of similar methods for calculating photoinduced CT rates in complex condensed-phase systems remains challenging.[24−28]

One exception is Marcus theory, which has offered an intuitive approach toward understanding CT rate constants in a wide range of condensed-phase systems,[29,30] as well as fitting and interpreting experimental measurements.[31] However, Marcus theory is based on the assumptions that the nuclear degrees of freedom (DOF) start out at thermal equilibrium on the donor electronic potential energy surface (PES) and that CT can be described by a rate constant. Under those conditions, the Marcus theory CT rate constant is expressed in terms of only three parameters: (1) electronic coupling coefficient, (2) reorganization energy, and (3) reaction free energy.[24] As such, Marcus theory provides a robust, flexible, and convenient platform for calculating CT rate constants in complex condensed-phase systems.[15,32−34] However, Marcus theory cannot account for the effects caused by the nonequilibrium nature of the initial state in photoinduced

CT. Such effects are expected to be important when the timescale of relaxation to thermal equilibrium on the donor PES is similar to or longer than the timescale on which the electronic transition occurs.[35,36]

In contrast, the nonequilibrium Fermi's golden rule (NE-FGR) is designed to account for effects caused by the nonequilibrium nature of the initial state.[37−42] Furthermore, combining the NE-FGR with the linearized semiclassical (LSC) approximation has made it possible to apply the NE-FGR to complex condensed-phase systems described by all-atom anharmonic Hamiltonians.[40,41] The LSC NE-FGR expression was also shown to coincide with the corresponding quantum-mechanically exact result when the donor and acceptor PESs correspond to multidimensional parabolas that differ only with respect to their equilibrium geometries and energies.[40] Furthermore, the time-dependent NE-FGR rate coefficient reduces to the time-independent equilibrium FGR (E-FGR) transition rate constant when the system starts out at equilibrium on the donor state and the electronic dephasing time is shorter than the electronic transition timescale. The

Marcus theory rate constant can then be obtained from the LSC approximation of the E-FGR by assuming that (1) the nuclear DOF are classical, (2) the nuclear motion occurs on a timescale slower than the electronic dephasing time, and (3) the equilibrium distribution of the donor–acceptor potential energy gap is Gaussian.[33,43]

Recently, we used the LSC E-FGR to estimate the CT rate constants between the three excited states of the carotenoid–porphyrin–C_{60} (CPC_{60}) molecular triad solvated in explicit tetrahydrofuran (THF).[44] It was found that the CT rate constants are strongly dependent on the conformation of the triad and that CT in the *linear* conformation is faster than in the *bent* conformation.[15,44] It was also found that CT is driven by the solvent DOF, rather than by the intramolecular triad DOF.[44] Here, the nuclear motion does not involve light particles and occurs at room temperature, so significant nuclear quantum effects are not expected; our recent study of mapping the all-atom Hamiltonians onto spin-boson models indeed showed very small nuclear quantum effects in this solution of triad in THF.[45]

In this paper, we apply the LSC NE-FGR to the above-mentioned solvated triad system to estimate the effects of nonequilibrium initial state preparation on the rate of photoinduced CT. To the best of our knowledge, this is the first-ever application of LSC NE-FGR to a condensed-phase system described by an all-atom anharmonic Hamiltonian. We also show that it is possible to derive the instantaneous Marcus theory (IMT, see below) from LSC NE-FGR by making several reasonable assumptions.

We assume that the triad is initially at equilibrium on the ground (G) state PES, CPC_{60}, before being impulsively photoexcited to the P-localized excitonic $\pi\pi*$ state, $CP*C_{60}$. Photoexcitation is then followed by either a transition to the excited P-to-C_{60} CT state, $CP^+C_{60}^-$, which is denoted as CT1

$$CPC_{60}(G) \xrightarrow{h\nu} CP*C_{60}(\pi\pi*) \rightarrow CP^+C_{60}^-(CT1) \qquad (1)$$
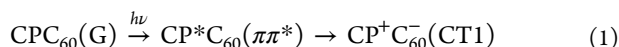
or to the excited C-to-C_{60} charge-separated state, $C^+PC_{60}^-$, which is denoted as CT2

$$CPC_{60}(G) \xrightarrow{h\nu} CP*C_{60}(\pi\pi*) \rightarrow C^+PC_{60}^-(CT2) \qquad (2)$$
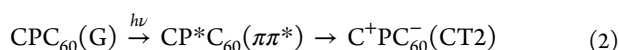
One-dimensional cartoons of the relevant PESs involved in these CT processes in two different triad conformations (bent and linear) are represented in Figure 1.

The remainder of this paper is organized as follows. Section 2 outlines the nonequilibrium Fermi's golden rule and instantaneous Marcus theory, respectively. The model and simulation techniques for the triad in THF are described in Section 3. Results are reported in Section 4. The conclusions and outlook are provided in Section 5.

2. THEORY

2.1. Nonequilibrium Fermi's Golden Rule. Consider a two-state system with the overall Hamiltonian $\hat{H} = \hat{H}_D|D\rangle\langle D| + \hat{H}_A|A\rangle\langle A| + \Gamma_{DA}(|D\rangle\langle A| + |A\rangle\langle D|)$, where $|D\rangle$ and $|A\rangle$ represent the diabatic donor and acceptor electronic states, respectively, and Γ_{DA} is the electronic coupling coefficient. $\hat{H}_{D/A}$ are the corresponding nuclear Hamiltonians, $\hat{H}_{D/A} = \hat{\mathbf{P}}^2/2 + V_{D/A}(\hat{\mathbf{R}})$, where $\hat{\mathbf{R}} = (\hat{R}_1,...,\hat{R}_N)$ and $\hat{\mathbf{P}} = (\hat{P}_1,...,\hat{P}_N)$ are the mass-weighted nuclear coordinates and momenta and $V_{D/A}(\hat{\mathbf{R}})$ are the donor/acceptor PESs (in what follows, boldfaced quantities correspond to vectors and quantities capped with ^ correspond to quantum-mechanical operators, while the same
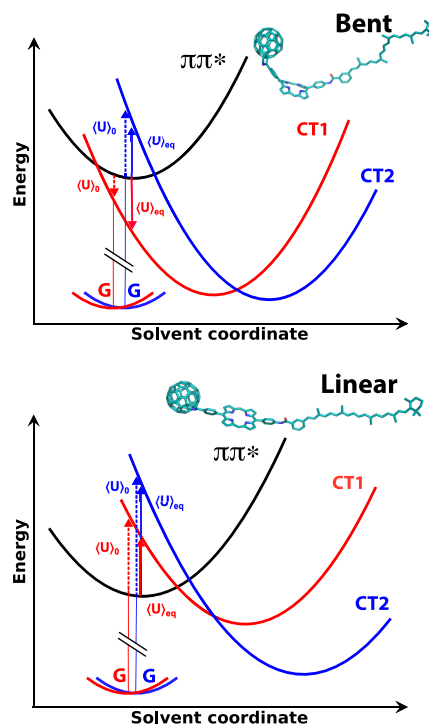

Figure 1. One-dimensional cartoons of the potential energy surfaces (PESs) for different donor-to-acceptor transitions between excited states after a vertical photoexcitation from the ground state in the bent (top) and linear (bottom) carotenoid–porphyrin–C_{60} (CPC_{60}) triad conformations. Here, $\langle U \rangle_{eq}$ is the average donor–acceptor potential energy gap sampled on the equilibrium donor ($\pi\pi*$) state, whereas $\langle U \rangle_0$ is the average donor–acceptor potential energy gap sampled on the equilibrium ground (G) state. The relative positions of the harmonic PESs are quantitatively obtained using the corresponding values of $\langle U \rangle_{eq}$, $\langle U \rangle_0$, and the reorganization energy E_r obtained from MD simulations performed on the all-atom anharmonic model of a rigid triad dissolved in THF.

quantities without ^ correspond to their classical counterparts).

Assuming that the system starts out at the donor electronic state with the state of the nuclear DOF described by the nuclear density operator $\hat{\rho}_0$ (in this paper, $\hat{\rho}_0$ is chosen to correspond to thermal equilibrium on the ground-state PES, $\hat{\rho}_0 = \hat{\rho}_G^{eq} = e^{-\beta\hat{H}_G}/Tr_n[e^{-\beta\hat{H}_G}]$, where $\hat{H}_G = \hat{\mathbf{P}}^2/2 + V_G(\hat{\mathbf{R}})$ is the ground-state nuclear Hamiltonian, $\beta = 1/k_B T$ is the inverse temperature, and $Tr_n(\cdot)$ denotes trace over the nuclear Hilbert space), the donor-state population $P_D(t)$ is given by

$$P_D(t) = Tr[e^{-i\hat{H}t/\hbar}\hat{\rho}_0 e^{i\hat{H}t/\hbar}|D\rangle\langle D|] \qquad (3)$$

where $Tr = Tr_n Tr_e$ denotes trace over both of the nuclear and electronic Hilbert spaces. Applying second-order perturbation theory, the donor-state population can be written as[37,40]

$$P_D(t) \approx \exp\left[-\int_0^t dt' k(t')\right] \qquad (4)$$

where the time-dependent rate coefficient is defined as

$$k(t') = \frac{2}{\hbar^2} Re \int_0^{t'} d\tau C(t',\tau) \qquad (5)$$

Here,

$$C(t',\tau) = |\Gamma_{DA}|^2 \text{Tr}_n[e^{-i\hat{H}_D t'/\hbar}\hat{\rho}_0 e^{i\hat{H}_D t'/\hbar} e^{-i\hat{H}_A \tau/\hbar} e^{i\hat{H}_D \tau/\hbar}] \quad (6)$$

For a detailed discussion of the LSC approximation of eq 6, as well as the progression of approximations that can be derived from it, the reader is referred to Appendix A and ref 40. The results presented in this paper were obtained at the "C-D" level of approximation, which corresponds to classical initial sampling and dynamics on the donor PES

$$C^{C-D}(t',\tau) = |\Gamma_{DA}|^2 \int d\mathbf{R}_0 d\mathbf{P}_0 \rho_0(\mathbf{R}_0, \mathbf{P}_0)$$
$$\times \exp\left[-\frac{i}{\hbar}\int_{t'}^{t'-\tau} dt\, U(\mathbf{R}_t^D)\right] \quad (7)$$

Here, $\rho_0(\mathbf{R}_0, \mathbf{P}_0)$ is the phase-space density that corresponds to the classical limit of $\hat{\rho}_0$, $U(\mathbf{R}) = V_D(\mathbf{R}) - V_A(\mathbf{R})$ is the donor−acceptor potential energy gap, and $\mathbf{R}_t^D$ is the nuclear configuration at time t, obtained via classical dynamics on the donor PES, starting with $(\mathbf{R}_0, \mathbf{P}_0)$ as the initial conditions. The nonequilibrium relaxation dynamics during t' is propagated on the donor PES at all levels of LSC NE-FGR. As we will show below, the results are not affected by our choice to perform the calculation at the C-D level, where the coherence dynamics during $(t', t' - \tau)$ occurs on the donor PES since the CT rates in the system under consideration turn out to be insensitive to the choice of PES that the coherence dynamics is based on.

We also note that starting with the nuclear DOF at thermal equilibrium on the donor PES, i.e., $\hat{\rho}_0 = \hat{\rho}_D^{eq} = e^{-\beta\hat{H}_D}/\text{Tr}_n[e^{-\beta\hat{H}_D}]$, implies that $C(t', \tau) \rightarrow C(\tau) = |\Gamma_{DA}|^2\text{Tr}_n[\hat{\rho}_D^{eq}e^{-i\hat{H}_A\tau/\hbar}e^{i\hat{H}_D\tau/\hbar}]$. Assuming that the donor-to-acceptor transition happens on a timescale longer than the lifetime of $C(\tau)$ then leads to $P_D(t) = \exp(-k_{D\rightarrow A}t)$, where $k_{D\rightarrow A}$ is the E-FGR rate constant given by[33]

$$k_{D\rightarrow A} = \frac{2}{\hbar^2}\text{Re}\int_0^\infty d\tau\, C(\tau)$$

$$C(\tau) = |\Gamma_{DA}|^2\text{Tr}_n[\hat{\rho}_D^{eq}e^{-i\hat{H}_A\tau/\hbar}e^{i\hat{H}_D\tau/\hbar}]$$
$$\approx |\Gamma_{DA}|^2\int d\mathbf{R}_0 d\mathbf{P}_0 \rho_D^{eq}(\mathbf{R}_0, \mathbf{P}_0)$$
$$\times \exp\left[\frac{i}{\hbar}\int_0^\tau dt\, U(\mathbf{R}_t^D)\right] \quad (8)$$

It should be noted that the *time-dependent rate coefficient* $k(t')$ replaces the *time-independent rate constant* $k_{D\rightarrow A}$ when the nuclear DOF start out at a nonequilibrium initial state. Accounting for this effect is important when $k(t')$ and $k_{D\rightarrow A}$ are significantly different and the timescale for reaching thermal equilibrium on the donor PES is comparable to or longer than the timescales of donor-to-acceptor electronic transition, $\sim k_{D\rightarrow A}^{-1}$. The last equality in eq 8 corresponds to the LSC approximation for the E-FGR at the C-D level.

The Marcus rate constant can be obtained from the LSC approximation of the E-FGR rate constant in eq 8 by replacing $C(\tau)$ by its second-order cumulant expansion and assuming that the lifetime of $C(\tau)$ is much shorter than the timescale of nuclear motion[33]

$$k_{D\rightarrow A}^{Marcus} = \frac{|\Gamma_{DA}|^2}{\hbar}\sqrt{\frac{2\pi}{\sigma^2}}\exp\left[-\frac{\langle U\rangle^2}{2\sigma^2}\right] \quad (9)$$

Here, $\langle U\rangle$ and σ are the average and standard deviation of the donor−acceptor potential energy gap U at equilibrium on the donor PES, respectively. The corresponding reorganization energy E_r and reaction free energy ΔE can be related to $\langle U\rangle$ and σ through the following relations: $E_r = \sigma^2/(2k_BT) = -\Delta E - \langle U\rangle$.

2.2. Instantaneous Marcus Theory. A more intuitive and quantitative way for understanding the trends in the transient CT rate is via the instantaneous Marcus theory (IMT) picture, where the transition rate coefficient, $k(t')$, is given in terms of the following Marcus-like expression with explicitly time-dependent donor−acceptor potential energy gap average and standard deviation

$$k^M(t') = \frac{|\Gamma_{DA}|^2}{\hbar}\sqrt{\frac{2\pi}{\sigma_{t'}^2}}\exp\left[-\frac{(\overline{U_{t'}})^2}{2\sigma_{t'}^2}\right] \quad (10)$$

Here, $\overline{U_{t'}}$ and $\sigma_{t'}$ are the nonequilibrium average and standard deviation of the donor−acceptor potential energy gap at time t' after the photoexcitation, respectively, which is calculated by averaging over many nonequilibrium trajectories that start out with the nuclear DOF sampled from $\rho_0(\mathbf{R}_0, \mathbf{P}_0)$ and whose dynamics is governed by the donor PES. Like the Marcus theory, the conditions under which the IMT expression is reasonably accurate are as follows: (1) the nuclear DOF are classical, (2) the nuclear motion occurs on a timescale slower than the electronic dephasing time, and (3) the t'-dependent distribution of the donor−acceptor potential energy gap is Gaussian.

The IMT rate coefficient in eq 10 can be derived starting from the LSC NE-FGR at the C-0 level[40]

$$C^{C-0}(t',\tau) = |\Gamma_{DA}|^2 \int d\mathbf{R}_0 d\mathbf{P}_0 \rho_0(\mathbf{R}_0, \mathbf{P}_0)$$
$$\times \exp\left[\frac{i}{\hbar}U(\mathbf{R}_{t'}^D)\tau\right]$$
$$\equiv |\Gamma_{DA}|^2\langle e^{iU_{t'}\tau/\hbar}\rangle \quad (11)$$

It should be noted that within this approximation, one would have a distribution of $U(\mathbf{R}_{t'}^D) = U_{t'}$ at each t' since each choice of $(\mathbf{R}_0, \mathbf{P}_0)$ will give rise to a different $\mathbf{R}_{t'}^D$. Substituting eq 11 into eq 6, we have

$$k^{C-0}(t') = \frac{2}{\hbar^2}\text{Re}\int_0^{t'} d\tau\, C^{C-0}(t',\tau)$$
$$= \frac{2}{\hbar^2}|\Gamma_{DA}|^2\text{Re}\int_0^{t'} d\tau\langle e^{iU_{t'}\tau/\hbar}\rangle \quad (12)$$

The integrand $\langle e^{iU_{t'}\tau/\hbar}\rangle$ is expected to decay to zero rapidly because the distribution of $U_{t'}$ will result in destructive interference (the broader the distribution, the faster the decay). The decay time can be easily estimated by calculating $\langle e^{iU_{t'}\tau/\hbar}\rangle$ directly from MD data. For the system under consideration, this decay time is ~20 fs (see Figure S2). Let $\tau_c(t')$ be the lifetime of $\langle e^{iU_{t'}\tau/\hbar}\rangle$ as a function of non-equilibrium time t'. Assuming that the lifetime $\tau_c(t')$ is much shorter on the timescale of nuclear motion, i.e., $t' > \tau_c(t')$ (which would be any timescale of practical interest in practice since τ_c is so short), we can then change the integration upper limit to infinity

Table 1. Comparison of E-FGR Marcus Rate Constants k^{M} (s^{-1}) and the NE-FGR Plateau Rate $k^{\mathrm{NE, \, plateau}}$ (s^{-1}) for Different CT Transitions in Flexible Bent (FB), Rigid Bent (RB), Flexible Linear (FL), and Rigid Linear (RL) Triad Solvated in Explicit THF[a]

transition	conf.	sampling	Γ_{DA}^2	$\langle U \rangle$	σ	k^{M}	$k^{\mathrm{NE, \, plateau}}$
$\pi\pi^* \rightarrow$ CT1	FB	G	5.8×10^{-4}	0.188	0.160	$6.9 \pm 0.2 \times 10^{12}$	
		$\pi\pi^*$		0.500	0.163	$1.6 \pm 0.1 \times 10^{11}$	$1.2 \pm 0.3 \times 10^{11}$
	RB	G	5.8×10^{-4}	0.163	0.161	$8.2 \pm 0.2 \times 10^{12}$	
		$\pi\pi^*$		0.471	0.161	$2.5 \pm 0.2 \times 10^{11}$	$1.8 \pm 0.7 \times 10^{11}$
	FL	G	8.1×10^{-5}	−0.175	0.182	$1.1 \pm 0.1 \times 10^{12}$	
		$\pi\pi^*$		−0.163	0.181	$1.1 \pm 0.1 \times 10^{12}$	$1.4 \pm 0.1 \times 10^{12}$
	RL	G	8.1×10^{-5}	−0.271	0.190	$6.0 \pm 0.1 \times 10^{11}$	
		$\pi\pi^*$		−0.218	0.190	$8.5 \pm 0.1 \times 10^{11}$	$5.6 \pm 0.4 \times 10^{11}$
$\pi\pi^* \rightarrow$ CT2	FB	G	2.0×10^{-9}	−0.563	0.271	$3.9 \pm 0.2 \times 10^{6}$	
		$\pi\pi^*$		−0.445	0.273	$7.7 \pm 0.3 \times 10^{6}$	$6.7 \pm 0.3 \times 10^{6}$
	RB	G	2.0×10^{-9}	−0.564	0.271	$4.1 \pm 0.2 \times 10^{6}$	
		$\pi\pi^*$		−0.416	0.272	$8.9 \pm 0.2 \times 10^{6}$	$6.9 \pm 0.2 \times 10^{6}$
	FL	G	4.0×10^{-8}	−0.409	0.297	$2.0 \pm 0.1 \times 10^{8}$	
		$\pi\pi^*$		−0.413	0.296	$1.9 \pm 0.1 \times 10^{8}$	$1.8 \pm 0.1 \times 10^{8}$
	RL	G	4.0×10^{-8}	−0.357	0.295	$2.5 \pm 0.1 \times 10^{8}$	
		$\pi\pi^*$		−0.365	0.295	$2.4 \pm 0.1 \times 10^{8}$	$2.4 \pm 0.1 \times 10^{8}$

[a]Here, Γ_{DA}^2 (eV^2) is the squared electronic coupling coefficient, and $\langle U \rangle$ (eV) and σ (eV) are the average and standard deviation of the donor−acceptor potential energy gap, respectively, obtained by sampling on the equilibrium ground (G) or $\pi\pi^*$ states.

$$
\begin{aligned}
k^{\mathrm{C-0}}(t') &= \frac{2}{\hbar^2} |\Gamma_{\mathrm{DA}}|^2 \, Re \int_0^\infty d\tau \langle e^{iU_{t'}\tau/\hbar} \rangle \\
&= \frac{1}{\hbar^2} |\Gamma_{\mathrm{DA}}|^2 \langle \int_{-\infty}^\infty d\tau e^{iU_{t'}\tau/\hbar} \rangle \\
&= \frac{2\pi}{\hbar} |\Gamma_{\mathrm{DA}}|^2 \langle \delta(U_{t'}) \rangle \\
&= \frac{2\pi}{\hbar} |\Gamma_{\mathrm{DA}}|^2 \, \mathrm{Prob}(U_{t'} = 0)
\end{aligned} \tag{13}
$$

Here, $\mathrm{Prob}(U_{t'} = 0)$ is the probability for $U_{t'} = 0$.

If we also assume that the instantaneous distribution of $U_{t'}$ is Gaussian, then

$$
\mathrm{Prob}(U; t') = \frac{1}{\sqrt{2\pi\sigma_{t'}^2}} \exp\left[-\frac{(U - \overline{U_{t'}})^2}{2\sigma_{t'}^2} \right] \tag{14}
$$

where $\overline{U_{t'}}$ is the nonequilibrium average of U and $\sigma_{t'} = \overline{U_{t'}^2} - (\overline{U_{t'}})^2$ is the corresponding standard deviation. Finally, inserting eq 14 into eq 13, we arrive at the IMT time-dependent rate coefficient as in eq 10.

The IMT rate coefficient $k^{\mathrm{M}}(t')$ can also be expressed in terms of time-dependent ΔE and E_r

$$
E_r(t') = \frac{\sigma_{t'}^2}{2k_{\mathrm{B}}T} = -\Delta E(t') - \overline{U_{t'}} \tag{15}
$$

It should be noted that similar expressions were proposed previously.[38,46,47] For example, Cho and Silbey derived an expression with a time-dependent reorganization energy but a constant σ^2 for harmonic systems,[46] which is different from eq 10. Also, Evans and Coalson arrived at an expression that is similar to our C-0 formula (eq 13).[38]

3. SIMULATION TECHNIQUES

The all-atom Hamiltonian of the CPC$_{60}$ molecular triad dissolved in THF was adopted from refs 15 and 44. For the bent and linear triad conformations, different force fields were constructed for the ground, $\pi\pi^*$, CT1, and CT2 states. The PESs for the entire system of the triad and THF differ from one electronic state to another by the excitation energies and the partial charges assigned to the triad atoms. The excitation energies, partial charges, and electronic coupling coefficients for this system were obtained from time-dependent density functional theory (TDDFT) using the range-separated hybrid BNL functional.[48−50] Although we are applying the Condon approximation by assuming the electronic coupling to be constant, in some sense, we take some non-Condon effects into account by assigning different electronic couplings to different triad conformations. For a given triad conformation, the Condon treatment is reasonable due to the fact that the low-amplitude solvent motion will not change the coupling dramatically. Partial charges for the triad on each electronic state on the donor-bridge-acceptor level and on the atomistic level are shown in Figures S3 and S4, respectively. Table S1 shows the energy corrections to the potential energy due to electronic excitation. The electronic coupling coefficients (Table 1) between the electronically excited states were assumed to be constant within the Condon approximation and calculated via the fragment charge difference (FCD) method.[51]

The potential energy of a triad in explicit THF solvent in the MD simulations consists of three terms: triad−triad $V_{\alpha, \mathrm{T}}(\mathbf{r})$, solvent−solvent $V_{\mathrm{S}}(\mathbf{s})$, and solvent−triad $V_{\alpha, \mathrm{ST}}(\mathbf{r}, \mathbf{s})$ interactions

$$
V_\alpha^{\mathrm{MD}}(\mathbf{r}, \mathbf{s}) = V_{\alpha, \mathrm{T}}(\mathbf{r}) + V_{\mathrm{S}}(\mathbf{s}) + V_{\alpha, \mathrm{ST}}(\mathbf{r}, \mathbf{s}) \tag{16}
$$

$$
V_{\alpha, \mathrm{T}}(\mathbf{r}) = V_{\mathrm{T}}^{\mathrm{NE}}(\mathbf{r}) + \sum_{j=1}^{n-1} \sum_{j'=j+1}^{n} \frac{1}{4\pi\varepsilon_0} \frac{q_j^\alpha q_{j'}^\alpha}{|\mathbf{r}_j - \mathbf{r}_{j'}|} \tag{17}
$$

$$
V_{\mathrm{S}}(\mathbf{s}) = V_{\mathrm{S}}^{\mathrm{NE}}(\mathbf{s}) + \sum_{i=1}^{N-1} \sum_{i'=i+1}^{N} \frac{1}{4\pi\varepsilon_0} \frac{Q_i Q_{i'}}{|\mathbf{s}_i - \mathbf{s}_{i'}|} \tag{18}
$$

$$
V_{\alpha, \mathrm{ST}}(\mathbf{r}, \mathbf{s}) = V_{\mathrm{TS}}^{\mathrm{NE}}(\mathbf{r}, \mathbf{s}) + \sum_{i=1}^{N} \sum_{j=1}^{n} \frac{1}{4\pi\varepsilon_0} \frac{Q_i q_j^\alpha}{|\mathbf{s}_i - \mathbf{r}_j|} \tag{19}
$$

Here, $\mathbf{R} = (\mathbf{r}, \mathbf{s})$, where $\mathbf{r}$ and $\mathbf{s}$ are the triad and solvent coordinates, respectively, α represents the electronic state of the triad (ground, $\pi\pi^*$, CT1, and CT2), $\{q_j^\alpha\}$ are the triad's

atomic partial charges (n atoms) in the α-th excited state, and $\{Q_i\}$ are the the solvent atomic partial charges (N atoms). The nonelectrostatic interaction terms, i.e., $V_T^{NE}(\mathbf{r})$, $V_S^{NE}(\mathbf{s})$, and $V_{ST}^{NE}(\mathbf{r}, \mathbf{s})$, are assumed to be the same for different electronic states.

The overall PES in the α-th excited state is given by[44]

$$V_\alpha(\mathbf{r}, \mathbf{s}) = V_\alpha^{MD}(\mathbf{r}, \mathbf{s}) + E_\alpha(\mathbf{r}^{G,eq}) - V_{\alpha,T}(\mathbf{r}^{G,eq})$$
$$= V_\alpha^{MD}(\mathbf{r}, \mathbf{s}) + W_\alpha \qquad (20)$$

Here, $E_\alpha(\mathbf{r}^{G,\,eq})$ is the α-th excited state energy with respect to the ground state for the gas-phase triad obtained from electronic structure calculations using the ground-state optimized or characteristic geometries, i.e., $\mathbf{r}^{G,\,eq}$ (in our case, bent and linear conformations). Since $V_\alpha^{MD}(\mathbf{r}, \mathbf{s}) + E_\alpha(\mathbf{r}^{G,\,eq})$ double counts the triad intramolecular interactions, we subtract the corresponding contribution from the classical force fields, $V_{\alpha,\,T}(\mathbf{r}^{G,\,eq})$, giving rise to the energy correction W_α to the MD potential energy at the α-th excited state. The values of E_α, $V_{\alpha,\,T}$, and W_α for the $\pi\pi^*$, CT1, and CT2 states in the bent and linear conformations are shown in Table S1. The donor−acceptor energy gap is thus given by

$$U(\mathbf{R}) = U(\mathbf{r}, \mathbf{s}) = V_D^{MD}(\mathbf{r}, \mathbf{s}) - V_A^{MD}(\mathbf{r}, \mathbf{s}) + (W_D - W_A) \qquad (21)$$

MD simulations for the system containing one triad molecule and 6741 THF molecules within a 100 Å × 100 Å × 100 Å periodic cubic simulation box were performed by the AMBER 18 package.[52] The general AMBER force field (GAFF)[53] was employed. We simulated four cases including flexible bent and flexible linear triad conformations, where the end-to-end distance between carbon atoms with indices of 21 and 193 as shown in Figure S1 (out of 207 atoms in the triad) was constrained at 49.6 Å using a harmonic force with a force constant of 100 kcal mol^{-1}Å^{-2} in the flexible linear conformation, as well as rigid bent and rigid linear triad conformations, where all atoms of the triad molecule were constrained using the same harmonic restraint. Particle mesh Ewald summation[54] was used to describe the long-ranged electrostatic interactions. All the covalent bonds involving hydrogen were constrained by the SHAKE algorithm.[55] A cutoff of 9.0 Å was employed for the van der Waals interactions. The MD time step was chosen as $\delta t = 1.0$ fs. The system was equilibrated at 300 K using a Langevin thermostat with a collision frequency of 1.0 ps^{-1}.

In the equilibrium MD simulations for the Marcus E-FGR rate constant calculation, 200 independent trajectories of 10 ns in length each were generated on the ground and $\pi\pi^*$ states' PESs in a constant-NVT ensemble, giving rise to 4×10^8 configurations in total, which were sampled every 5 fs.

In the nonequilibrium MD simulations for NE-FGR and IMT calculations, 2×10^4 independent initial configurations were sampled from a constant-NVT ensemble at 300 K on the ground-state PES. Subsequently, 2×10^4 nonequilibrium trajectories were generated on the $\pi\pi^*$ state PES in the constant-NVE ensemble of 4 ps in length with a time step of 1.0 fs, and 4000 configurations and energy gaps ($\pi\pi^* \to$ CT1 and $\pi\pi^* \to$ CT2) were recorded per trajectory with a time interval of one time step between frames. Thus, a sum total of 8×10^7 nonequilibrium configurations were averaged over, obtaining the NE-FGR and IMT rates. The NE-FGR plateau values for each transition were obtained by dividing 2×10^4 trajectories into five blocks, and the plateau value of each block

was calculated from $t' = 3$ to 4 ps. The NE-FGR plateau values of the five blocks and their average with error bars are provided in Table S2.

Finally, we estimate the computational cost for the nonequilibrium MD simulations for NE-FGR or IMT calculation. For each nonequilibrium trajectory, generating 4000 configurations and recalculating the potential energies on all states ($\pi\pi^*$, CT1, and CT2) take about 21 min on an HPC node with two Intel Xeon Gold 6132 @ 2.60 GHz (28 cores) CPUs using the Sander module in AMBER 18. Thus, the total computational cost of nonequilibrium MD simulations for the four cases of triad conformations studied in this paper is about 784,000 core-hours, which is expensive. Therefore, it would be desirable to develop an efficient method for these types of calculations. Work in this direction is underway and will be reported in a separate future publication.

4. RESULTS AND DISCUSSION

We present results for two characteristic conformations of the triad, bent and linear, with the intramolecular triad DOF either
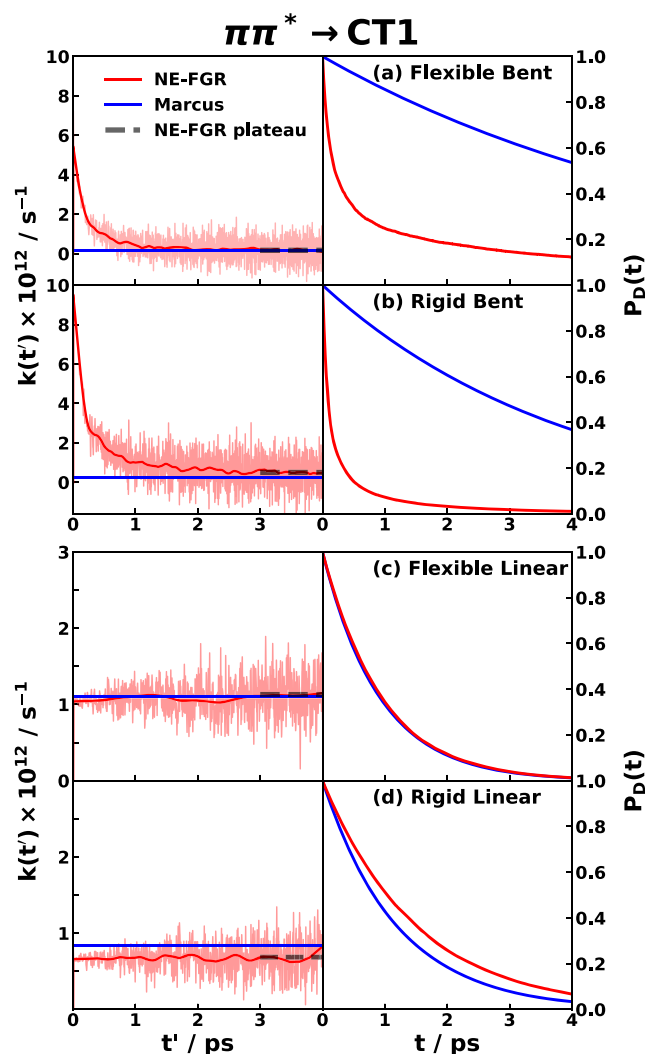

Figure 2. NE-FGR rate coefficient (left) and donor-state population (right) for the $\pi\pi^*\to$CT1 transition in (a) the flexible bent, (b) rigid bent, (c) flexible linear, and (d) rigid linear triad cases, in comparison with E-FGR Marcus rate constants (blue). The dashed lines indicate the NE-FGR plateau.
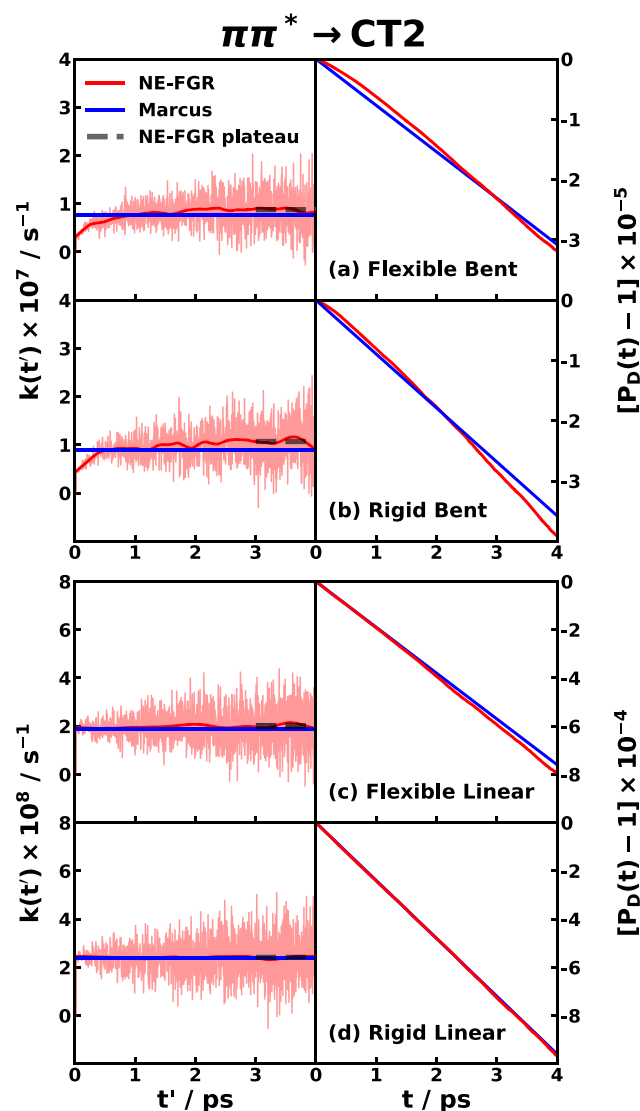
Figure 3. NE-FGR rate coefficient (left) and donor-state population (right) for the $\pi\pi^* \to CT2$ transition in (a) the flexible bent, (b) rigid bent, (c) flexible linear, and (d) rigid linear triad cases, in comparison with E-FGR Marcus rate constants (blue). The dashed lines indicate the NE-FGR plateau.

frozen (rigid) or flexible. The point of considering two conformations is to elucidate the correlation between the molecular structure and CT rates. The point of considering the rigid and flexible cases is to elucidate whether or not the intramolecular motions of the triad contribute to the CT process.

NE-FGR transition rate coefficients, $k(t')$, and donor population relaxation profiles, $P_D(t)$, as calculated for the $\pi\pi^* \to CT1$ transition via the LSC approximation at the C-D level (eq 7), are shown in the left and right panels of Figure 2, respectively. Also shown in Figure 2 are the corresponding predictions based on E-FGR at the Marcus theory level (eq 9). Significant deviations between the predictions of E-FFR and NE-FGR are observed in the bent conformation, where the population of the donor $\pi\pi^*$ state is seen to drop by ~90% within the first ~1 ps, which is the timescale for $k(t')$ to reach its plateau value. Importantly, reaching the plateau corresponds to reaching thermal equilibrium on the donor PES. It should also be noted that the plateau value agrees with the Marcus

rate constant calculated with sampling on equilibrium donor PES (see Table 1). In other words, the system is in a nonequilibrium state during the initial ~1 ps transient period during which ~90% of the CT process is completed. Thus, the $\pi\pi^* \to CT1$ transition in the bent conformation is seen to follow nonexponential kinetics (as manifested by the strong time dependence of the transition coefficient, $k(t')$) and to be strongly enhanced by the nonequilibrium nature of the initial state.

It should also be noted that the relaxation timescale and the plateau value of the $\pi\pi^* \to CT1$ transition rate in the bent conformation are relatively insensitive to whether the triad intramolecular DOF contribute (flexible) or not (rigid). This has already been observed for Marcus theory rate constants in ref 44. However, the initial rate coefficient in the rigid bent triad is higher than that in the flexible bent triad, which can be traced back to structural differences in the equilibrated ground state. These observations suggest that this transient CT process is dominated by the intermolecular (solvent) DOF, rather than by the intramolecular (triad) DOF. Importantly, the results in Figure 2 show that the intermolecular solvent DOF also dominate the photoinduced CT processes when the system starts out in a nonequilibrium state.

The nonequilibrium nature of the initial state is seen to have a very different effect on the $\pi\pi^* \to CT1$ transition rate in the linear conformation (see Figure 2c,d). In this case, the deviations between the E-FGR and NE-FGR rates are rather modest in the transient period. It should also be noted that the NE-FGR plateau value in the case of the rigid linear triad is somewhat different from the Marcus theory rate constant. This suggests either deviations from the Marcus limit or that equilibrium on the donor PES has not been reached yet within the 4 ps simulation time window. However, the deviations from thermal equilibrium do not lead to significant deviations in CT rates and exponential kinetics in this case.

The fact that both the timescale and kinetics of the $\pi\pi^* \to CT1$ transition are strongly conformation-dependent can be viewed as a structure−function relation, where the molecular structure (triad conformation) is seen to have a rather dramatic effect on the function (the CT rate). Thus, the triad provides a relatively simple demonstration for the potential importance of such structure−function relations in more complex systems, such as the correlation between interfacial structure and interfacial CT rates in OPV materials.[13,56,57]

Next, NE-FGR transition coefficients, $k(t')$, and donor population relaxation profiles, $P_D(t)$, as calculated for the $\pi\pi^* \to CT2$ transition via the LSC approximation at the C-D level (eq 7), are shown in the left and right panels of Figure 3, respectively. Results are shown for the bent and linear conformations, with the intramolecular triad DOF frozen (rigid) or flexible. Also shown in Figure 3 are the corresponding predictions based on E-FGR at the Marcus theory level (eq 9). In contrast to the $\pi\pi^* \to CT1$ transition, the nonequilibrium nature of the initial state has a negligible effect on the $\pi\pi^* \to CT2$ transition rate. This can be traced back to the fact that the $\pi\pi^* \to CT2$ transition is much slower, as is evident by the fact that only 10^{-5} of the donor population is lost within the initial 4 ps (compare to Figure 2, where much of the donor population has transferred to the acceptor state on the same timescale). This means that the equilibration process of the nuclear DOF on the donor PES, which occurs on the picosecond timescale, would have little effect on the overall CT rate. In both cases, the extremely minor
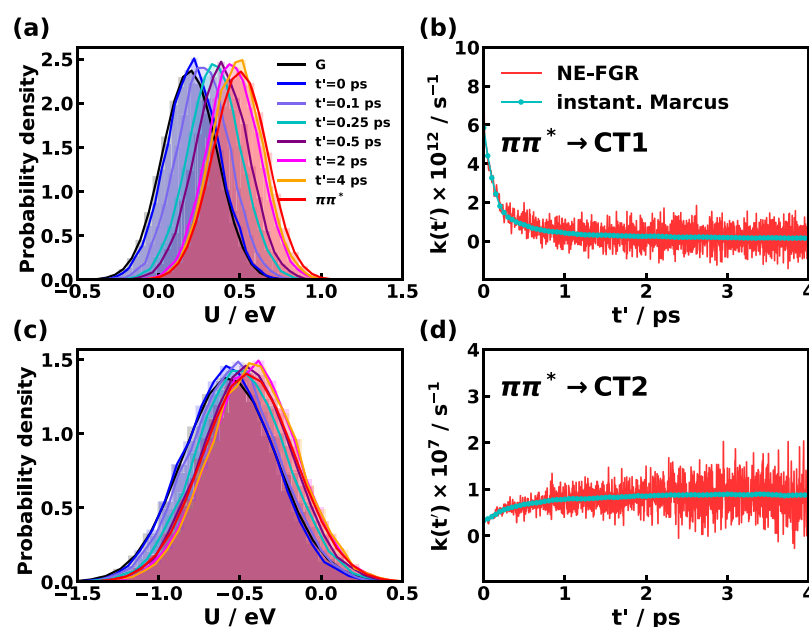
Figure 4. Distribution of energy gap (U) for (a) the $\pi\pi^*\rightarrow$CT1 transition and (c) $\pi\pi^*\rightarrow$CT2 transition in the flexible bent triad at different times after the vertical excitation from the ground state and (b, d) the corresponding instantaneous Marcus rate coefficient (cyan) and NE-FGR rate coefficient (red).
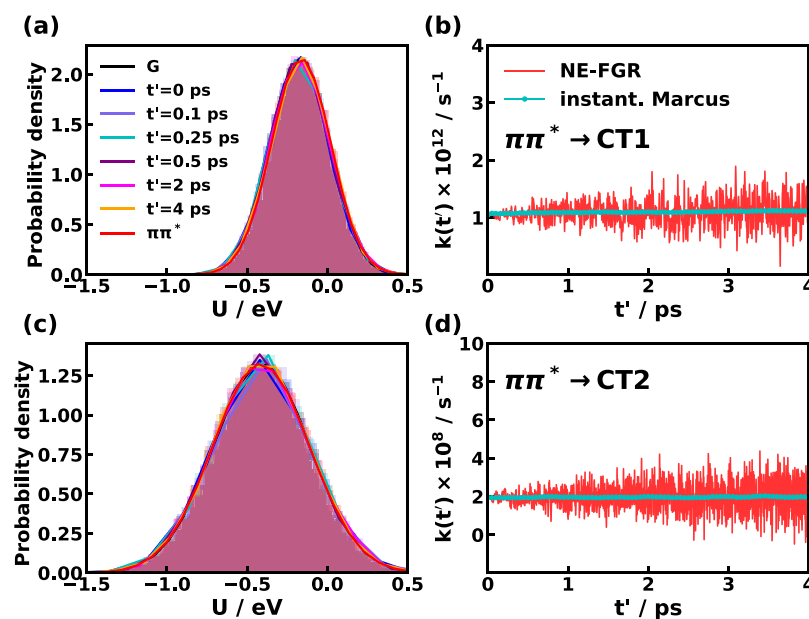

Figure 5. Distribution of energy gap (U) of (a) the $\pi\pi^*\rightarrow$CT1 transition and (c) $\pi\pi^*\rightarrow$CT2 transition in the flexible linear triad at different times after the vertical excitation from the ground state and (b, d) the corresponding instantaneous Marcus rate coefficient (cyan) and NE-FGR rate coefficient (red).

nonequilibrium effects that can be observed are more pronounced in the bent conformation.

The above trends in the CT rate coefficients are consistent with and can be understood in terms of the PESs in Figure 1, which are drawn to scale for the case of the rigid triad. For the $\pi\pi^*\rightarrow$CT1 process in the bent conformation, one observes that the deviation of the nonequilibrium initial state of the nuclear DOF from the corresponding equilibrium state is the largest, which would lead to stronger nonequilibrium effects. Furthermore, the nonequilibrium initial state of the nuclear DOF is in closer proximity to the crossing region between the $\pi\pi^*$ and CT1 PESs, which leads to the observed enhancement

in the CT rate. At the same time, the deviation of the nonequilibrium initial state of the nuclear DOF from the corresponding equilibrium state is much smaller in the case of the $\pi\pi^*\rightarrow$CT1 process in the linear conformation than in the bent conformation, which leads to less pronounced nonequilibrium effects. Furthermore, the fact that the nuclear configuration is further away from the crossing region between the $\pi\pi^*$ and CT1 PESs in the initial nonequilibrium state than it is in thermal equilibrium is consistent with the fact that the NE-FGR is in fact somewhat slower in comparison to the Marcus rate constant.
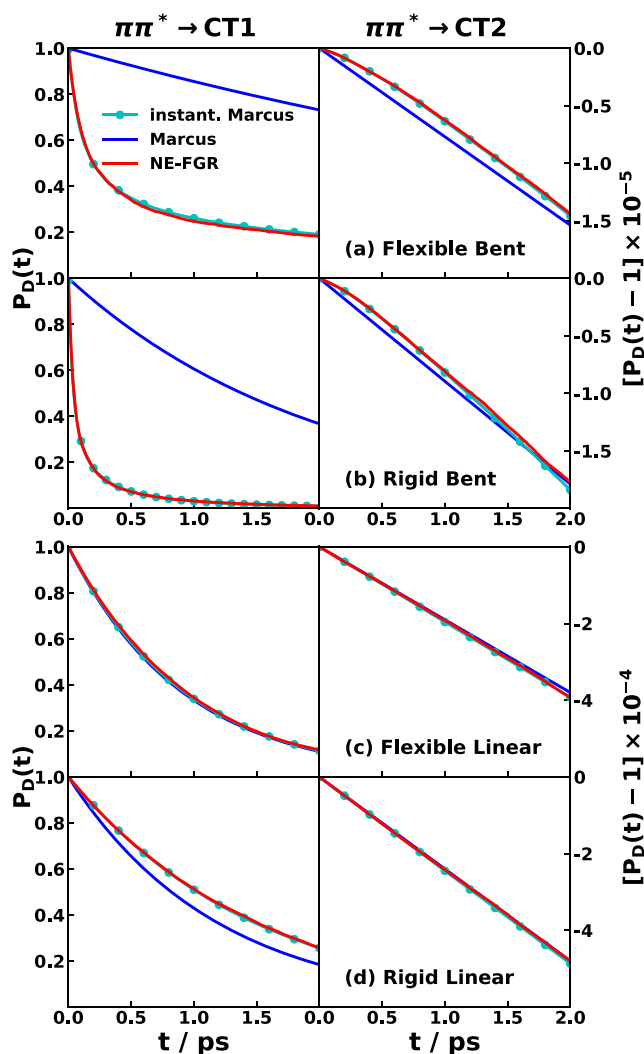
Figure 6. Comparison of instantaneous Marcus theory (cyan), Marcus theory (blue), and NE-FGR (red) for the donor population decay in $\pi\pi^*\rightarrow$CT1 and $\pi\pi^*\rightarrow$CT2 transitions with initial sampling on the ground state in different triad conformations.

Figure 7. Time dependence of U, σ, E_r, $|\Delta E|$, and E_A obtained from the nonequilibrium MD simulations on the $\pi\pi^*$ PES, starting with equilibrium ground state for flexible bent (FB), rigid bent (RB), flexible linear (FL), and rigid linear (RL) triad cases.

For the $\pi\pi^*\rightarrow$CT2 process, the deviations of the non-equilibrium initial state of the nuclear DOF from the corresponding equilibrium state are rather small in both bent and linear conformations. This fact, combined with the overall slower rate compared to the $\pi\pi^*\rightarrow$CT1, then leads to negligible nonequilibrium effects.

The IMT rate coefficients are found to be in excellent agreement with the corresponding LSC NE-FGR rate coefficients at the C-D level, as shown in Figure 4b,d, in the cases of $\pi\pi^*\rightarrow$CT1 and $\pi\pi^*\rightarrow$CT2 transitions in the flexible bent case. It should be noted that obtaining the IMT rate coefficients is also computationally more cost-effective. This can be traced back to the fact that calculating the rate coefficient based on eq 7 requires numerically averaging over an oscillatory integrand, whereas the same integration can be performed analytically when the energy gap distribution is Gaussian. Similar excellent agreement between IMT and LSC NE-FGR at the C-D-level CT rate coefficients is shown in Figure 5 and Figures S5 and S6 for the flexible linear, rigid bent, and rigid linear cases, respectively. Figure S7 shows that the energy gap distributions at different times are Gaussian, thereby validating the underlying assumptions in IMT. Figure
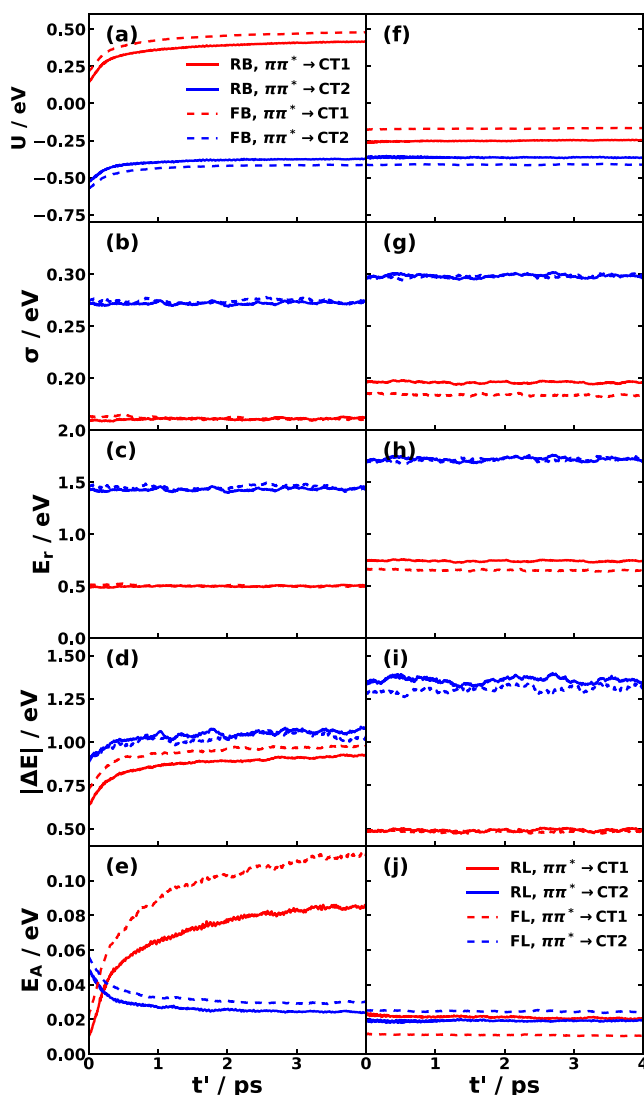
6 shows the excellent agreement of donor-state population decay between IMT and NE-FGR approaches in all the cases investigated here.

The IMT also provides a way to interpret the non-equilibrium effects on the molecular level via the time dependence of $\overline{U}_{t'}$, $\sigma_{t'}$, $E_r(t')$, $\Delta E(t')$, and $E_A(t')$. In the case of the rigid bent triad shown in Figure 7a,b, $\overline{U}_{t'}$ is seen to increase, while $\sigma_{t'}$ is seen to be constant with increasing t', which implies that the corresponding instantaneous activation energy, $E_A(t') = k_B T(\overline{U}_{t'})^2/(2\sigma_{t'}^2)$, increases and, therefore, $k^M(t')$ decreases with increasing t'. More specifically, for $\pi\pi^*\rightarrow$ CT1, $\overline{U}_{t'}$ increases from about 0.2 to 0.3 eV and $\sigma_{t'}$ fluctuates around 0.16 eV over the first 4 ps. This translates into an increase in E_A from about 0.015 to 0.08 eV, thereby diminishing the CT rate coefficient with increasing t'. At the same time, for the $\pi\pi^*\rightarrow$CT2 transition, $\overline{U}_{t'}$ increases from -0.5 to -0.4 eV and $\sigma_{t'}$ fluctuates around 0.27 eV over the first 4 ps, which translates into a decrease in E_A from about 0.05 to
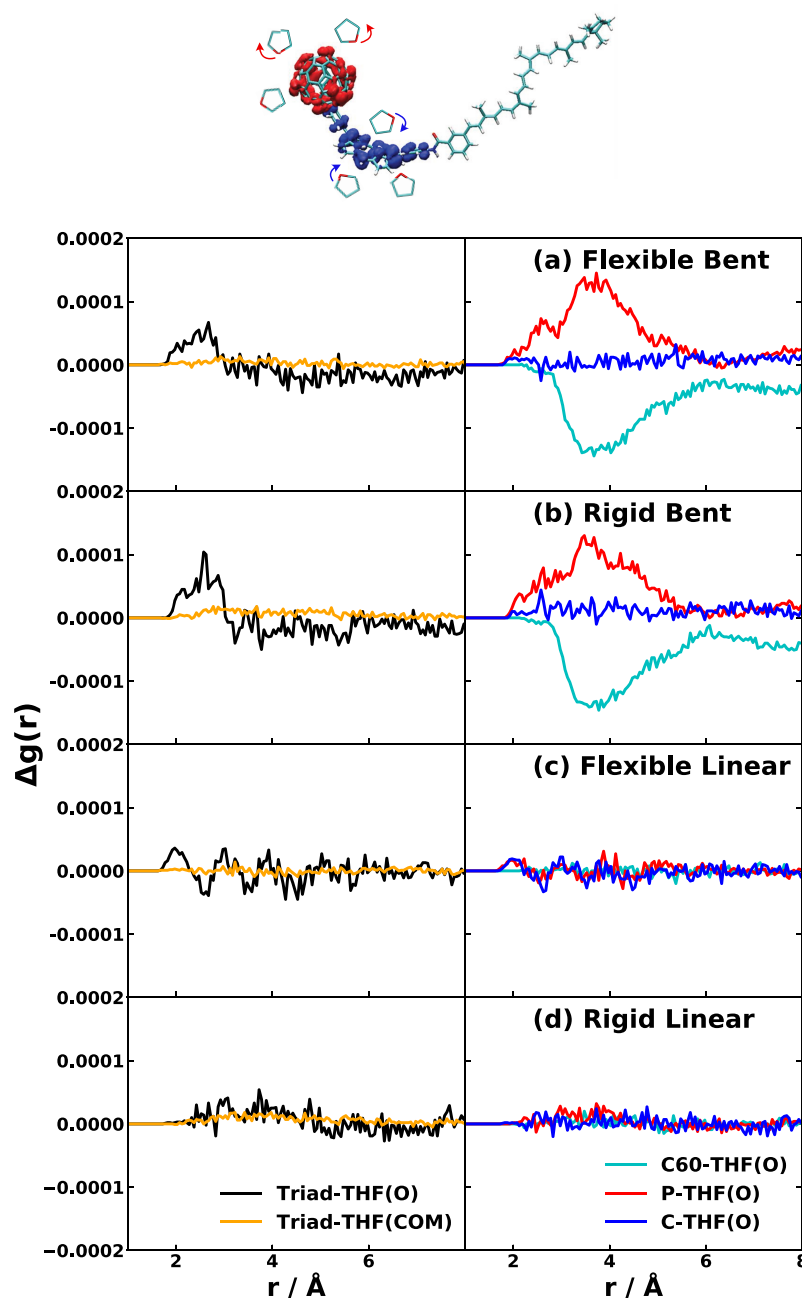
Figure 8. Difference in the radial distribution function $\Delta g(r)$ of the distance between the triad and THF between 4 and 0 ps after the photoexcitation, as obtained from nonequilibrium MD simulations in (a) the flexible bent, (b) rigid bent, (c) flexible linear, and (d) rigid linear triad cases. Top: illustration of solvent reorientation for bent triad. Left panels: triad surface and oxygen atom of THF (black) and triad surface and center of mass of THF (orange). Right panels: the C_{60} part (cyan), porphyrin (P) part (red), and carotenoid (C) part (blue) of triad and oxygen of THF contributions.

0.03 eV and, therefore, an increase in $k^M(t')$ with increasing t' (see bottom panels in Figure 7).

The above-mentioned trends in $\overline{U_{t'}}$, which corresponds to the center of the distribution over U at time t', are consistent with Figure 7. For example, since the deviation of the initial value of $\langle U \rangle_0$ from $\langle U \rangle_{eq}$ for the $\pi\pi^* \rightarrow CT1$ transition in the bent conformation is larger than that for the $\pi\pi^* \rightarrow CT2$ transition, relaxation on the donor ($\pi\pi^*$) PES leads to a larger change in the case of the $\pi\pi^* \rightarrow CT1$ transition.

The above-mentioned trends in $\sigma_{t'}$ can be understood based on the underlying nonequilibrium solvation dynamics. The phenomenon that $\sigma_{t'}$ for $\pi\pi^* \rightarrow CT2$ is in general larger than

for $\pi\pi^* \rightarrow CT1$ can be traced back to the fact that CT2 is associated with CT over a longer distance. As a result, the difference in potential energy relative to the $\pi\pi^*$ state is larger on average and so is its fluctuation because more solvent molecules are directly affected by charge separation over a longer distance.

The solvation process can be visualized by looking at the time evolution of the corresponding radial distribution functions (RDFs) between the triad surface and the THF molecules. As shown in Figure 8, for the bent triad, the difference in the RDF between the triad and THF centers of mass right on the time of the photoexcitation and the RDF at 4

ps after photoexcitation, $\Delta g(r)$, shows almost no changes, while the difference in the RDF between the triad and negatively charged oxygen atom in THF (black lines) shows an incremental shift from ~3.0–6.0 to ~2.0–3.0 Å near the first solvation shell. This solvation dynamics is driven by the difference in partial charge of the ground state and $\pi\pi^*$ state for the bent triad, as shown in Figure S3. By examining the contributions from different parts of the triad, it is evident that a more structured solvation shell is formed, as can be observed from the increased RDF between the negatively charged C_{60} part and the oxygen in THF (cyan) and the decreased RDF between the positively charged porphyrin part and the oxygen in THF (red) (see Figure 8, right panels). This structural rearrangement gives rise to a picture of reorientation of the THF molecules so as to align their dipoles in a manner that leads to stabilization on the $\pi\pi^*$ PES (see top illustration of Figure 8), which corresponds to even lower potential energies on the CT surfaces and thus an increase in the donor–acceptor energy gap.

However, it should be pointed out that the change in the RDF around the first solvation shell is relatively small compared with the entire first shell total height. The structural reorientation is rather a small effect but would be helpful for understanding the energetic change in the relaxation process. The linear triad shows no change in the RDFs, therefore no significant change in the energy gap.

5. CONCLUDING REMARKS

We applied the LSC NE-FGR to calculate the photoinduced CT dynamics in the CPC_{60} molecular triad dissolved in explicit THF. To the best of our knowledge, this is the first application of the LSC NE-FGR to a condensed-phase system described by an all-atom anharmonic Hamiltonian. For this system, we calculated the time-dependent electronic transition rate coefficients from the porphyrin-localized $\pi\pi^*$ state (CP^*C_{60}) to the porphyrin-to-C_{60} charge transfer state ($CP^+C_{60}^-$), or the carotenoid-to-C_{60} charge-separated state ($C^+PC_{60}^-$), in two different conformations (bent and linear). The initial nonequilibrium state corresponds to impulsive photoexcitation from the equilibrated ground state to the $\pi\pi^*$ state. Our NE-FGR calculations show that the nonequilibrium nature of the initial state can lead to significant deviations of the CT rate in comparison to the case where the system is assumed to start out at equilibrium on the donor PES as in E-FGR. More specifically, we find that the $CP^*C_{60} \rightarrow CP^+C_{60}^-$ transition rate in the bent conformation is 40 times faster when nonequilibrium effects are accounted for. While we are not aware of direct experimental evidence for the transient nonequilibrium effects reported in this paper, we believe that such evidence may be obtainable from pump-probe measurements. We also showed that the results are consistent with the IMT, which the LSC NE-FGR rate coefficient can be shown to reduce into for the system under consideration. Within IMT, the transition rate coefficient is given by a Marcus-like expression, with explicitly time-dependent donor–acceptor energy gap average and standard deviation or equivalently time-dependent reorganization energy and reaction free energy.

The LSC NE-FGR and IMT open the door to the investigation of nonequilibrium effects on CT and energy transfer rates in many systems of current technological and biological interest, including confined molecular systems,[58] condensed-phase systems,[59] and semiconductor interfaces.[57]

Work on such extensions is underway and will be reported in future publications.

■ APPENDIX A

A.1. Hierarchy of Linearized Semiclassical NE-FGR

In this appendix, we outline the hierarchy of linearized semiclassical (LSC) approximations to the nonequilibrium Fermi's golden rule (NE-FGR) that was developed in the previous work.[40] LSC is based on expressing the correlation function as a real-time path integral and then applying the linearization approximation to the differences in the forward and backward paths. Adding additional approximations then leads to more cost-effective approximations, which eventually leads to the instantaneous Marcus theory (IMT) introduced in the main text.

The hierarchy of LSC-based expressions for NE-FGR $C(t', \tau)$ with arbitrary initial preparation dictated by $\hat{\rho}_0$ is given by

$$C^{\text{W-AV}}(t',\tau) = |\Gamma_{\text{DA}}|^2 \int d\mathbf{R}_0 d\mathbf{P}_0 [\hat{\rho}_0]_{\text{W}}(\mathbf{R}_0, \mathbf{P}_0)$$
$$\times \exp\left[-\frac{i}{\hbar} \int_{t'}^{t'-\tau} d\tau U(\mathbf{R}_t^{\text{av}})\right] \tag{A.1}$$

$$C^{\text{W-0}}(t',\tau) = |\Gamma_{\text{DA}}|^2 \int d\mathbf{R}_0 d\mathbf{P}_0 [\hat{\rho}_0]_{\text{W}}(\mathbf{R}_0, \mathbf{P}_0)$$
$$\times \exp\left[\frac{i}{\hbar} U(\mathbf{R}_{t'})\tau\right] \tag{A.2}$$

$$C^{\text{C-AV}}(t',\tau) = |\Gamma_{\text{DA}}|^2 \int d\mathbf{R}_0 d\mathbf{P}_0 \rho_0(\mathbf{R}_0, \mathbf{P}_0)$$
$$\times \exp\left[-\frac{i}{\hbar} \int_{t'}^{t'-\tau} d\tau U(\mathbf{R}_\tau^{\text{av}})\right] \tag{A.3}$$

$$C^{\text{C-D}}(t',\tau) = |\Gamma_{\text{DA}}|^2 \int d\mathbf{R}_0 d\mathbf{P}_0 \rho_0(\mathbf{R}_0, \mathbf{P}_0)$$
$$\times \exp\left[-\frac{i}{\hbar} \int_{t'}^{t'-\tau} d\tau U(\mathbf{R}_\tau^{\text{D}})\right] \tag{A.4}$$

$$C^{\text{C-0}}(t',\tau) = |\Gamma_{\text{DA}}|^2 \int d\mathbf{R}_0 d\mathbf{P}_0 \rho_0(\mathbf{R}_0, \mathbf{P}_0)$$
$$\times \exp\left[\frac{i}{\hbar} U(\mathbf{R}_{t'})\tau\right] \tag{A.5}$$

Here, "W" denotes Wigner sampling for nuclear DOF

$$[\hat{\rho}_0]_{\text{W}}(\mathbf{R}_0, \mathbf{P}_0) = \left(\frac{1}{2\pi\hbar}\right)^N \int d\mathbf{Z} e^{i\mathbf{Z}\cdot\mathbf{P}/\hbar}$$
$$\times \langle \mathbf{R} - \mathbf{Z}/2|\hat{\rho}_0|\mathbf{R} + \mathbf{Z}/2\rangle \tag{A.6}$$

"C" denotes classical nuclear sampling via the corresponding classical distribution $\rho_0(\mathbf{R}_0, \mathbf{P}_0)$ following the initial sampling. In the all-atom simulations, after sampling initial conditions $(\mathbf{R}_0, \mathbf{P}_0)$ via Wigner or classical nuclear densities, the system is propagated on the donor surface forward for time t', arriving at $\mathbf{R}_{t'}$, and then backward from time t' to $t' - \tau$ ($\tau = 0 \rightarrow t'$), integrating the energy gap in the phase factor, for each point in $C(t', \tau)$, where "AV" denotes that the τ-dynamics is propagated

on the average surface $V_{av} = (V_D + V_A)/2$, resulting in trajectories of $\mathbf{R}_t^{av}$, "D" denotes the τ-dynamics on the donor surface, resulting in trajectories of $\mathbf{R}_\tau^D$, and "0" denotes no τ-dynamics beyond the relaxation on donor PES until $\mathbf{R}_{t'}$.

■ ASSOCIATED CONTENT

ⓈⒾ Supporting Information

The Supporting Information is available free of charge at https://pubs.acs.org/doi/10.1021/acs.jpcb.0c06306.

Energy correction W_α defined as the difference between the excitation energy E_α and triad-only MD potential energy $V_{\alpha,T}$ for each excited state; NE-FGR CT rate plateau value ($k^{NE,plateau}$) and its error bars by averaging five blocks of data; Marcus rate constants for the triad (k^M in unit of s^{-1}) for different transitions; two conformations of the CPC_{60} triad; $\langle e^{iU_t \tau/\hbar} \rangle$ calculated by averaging over 20,000 $U_{t'}$ sampled from the nonequilibrium MD simulations at different time t' (PDF)

■ AUTHOR INFORMATION

Corresponding Author

Xiang Sun − Division of Arts and Sciences, NYU Shanghai, Shanghai 200122, China; NYU-ECNU Center for Computational Chemistry at NYU Shanghai, Shanghai 200062, China; Department of Chemistry, New York University, New York, New York 10003, United States; Ⓞ orcid.org/0000-0002-2846-8532; Email: xiang.sun@nyu.edu

Authors

Zhubin Hu − Division of Arts and Sciences, NYU Shanghai, Shanghai 200122, China; NYU-ECNU Center for Computational Chemistry at NYU Shanghai, Shanghai 200062, China; Ⓞ orcid.org/0000-0001-8490-3773

Zhengqing Tong − Division of Arts and Sciences, NYU Shanghai, Shanghai 200122, China; NYU-ECNU Center for Computational Chemistry at NYU Shanghai, Shanghai 200062, China; Ⓞ orcid.org/0000-0002-2146-7596

Margaret S. Cheung − Department of Physics, University of Houston, Houston, Texas 77204, United States; Ⓞ orcid.org/0000-0001-9235-7661

Barry D. Dunietz − Department of Chemistry and Biochemistry, Kent State University, Kent, Ohio 44242, United States; Ⓞ orcid.org/0000-0002-6982-8995

Eitan Geva − Department of Chemistry, University of Michigan, Ann Arbor, Michigan 48109, United States; Ⓞ orcid.org/0000-0002-7935-4586

Complete contact information is available at:
https://pubs.acs.org/10.1021/acs.jpcb.0c06306

Notes

The authors declare no competing financial interest.

■ ACKNOWLEDGMENTS

■ REFERENCES

(1) Muegge, I.; Qi, P. X.; Wand, A. J.; Chu, Z. T.; Warshel, A. The Reorganization Energy of Cytochrome c Revisited. *J. Phys. Chem. B* **1997**, *101*, 825−836.

(2) Voityuk, A. A. Effects of Dynamic Disorder on Exciton Delocalization and Photoinduced Charge Separation in DNA. *Photochem. Photobiol. Sci.* **2013**, *12*, 1303−1309.

(3) Scholes, G. D.; Fleming, G. R.; Olaya-Castro, A.; Van Grondelle, R. Lessons from Nature About Solar Light Harvesting. *Nat. Chem.* **2011**, *3*, 763.

(4) Cupellini, L.; Calvani, D.; Jacquemin, D.; Mennucci, B. Charge Transfer from the Carotenoid Can Quench Chlorophyll Excitation in Antenna Complexes of Plants. *Nat. Commun.* **2020**, *11*, 662−668.

(5) Akimov, A. V.; Neukirch, A. J.; Prezhdo, O. V. Theoretical Insights into Photoinduced Charge Transfer and Catalysis at Oxide Interfaces. *Chem. Rev.* **2013**, *113*, 4496−4565.

(6) Liddell, P. A.; Kuciauskas, D.; Sumida, J. P.; Nash, B.; Nguyen, D.; Moore, A. L.; Moore, T. A.; Gust, D. Photoinduced Charge Separation and Charge Recombination to a Triplet State in a Carotene−Porphyrin−Fullerene Triad. *J. Am. Chem. Soc.* **1997**, *119*, 1400−1405.

(7) Liddell, P. A.; Kodis, G.; Moore, A. L.; Moore, T. A.; Gust, D. Photonic Switching of Photoinduced Electron Transfer in a Dithienylethene−Porphyrin−Fullerene Triad Molecule. *J. Am. Chem. Soc.* **2002**, *124*, 7668−7669.

(8) Brédas, J.-L.; Beljonne, D.; Coropceanu, V.; Cornil, J. Charge-Transfer and Energy-Transfer Processes in π-Conjugated Oligomers and Polymers: A Molecular Picture. *Chem. Rev.* **2004**, *104*, 4971−5004.

(9) Tian, H.; Yu, Z.; Hagfeldt, A.; Kloo, L.; Sun, L. Organic Redox Couples and Organic Counter Electrode for Efficient Organic Dye-sensitized Solar Cells. *J. Am. Chem. Soc.* **2011**, *133*, 9413−9422.

(10) Mishra, A.; Fischer, M. K. R.; Bäuerle, P. Metal-Free Organic Dyes for Dye-Sensitized Solar Cells: From Structure: Property Relationships to Design Rules. *Angew. Chem., Int. Ed.* **2009**, *48*, 2474−2499.

(11) Feldt, S. M.; Gibson, E. A.; Gabrielsson, E.; Sun, L.; Boschloo, G.; Hagfeldt, A. Design of Organic Dyes and Cobalt Polypyridine Redox Mediators for High-Efficiency Dye-Sensitized Solar Cells. *J. Am. Chem. Soc.* **2010**, *132*, 16714−16724.

(12) Lee, M. H.; Dunietz, B. D.; Geva, E. Calculation from First Principles of Intramolecular Golden-Rule Rate Constants for Photo-Induced Electron Transfer in Molecular Donor−Acceptor Systems. *J. Phys. Chem. C* **2013**, *117*, 23391−23401.

(13) Lee, M. H.; Geva, E.; Dunietz, B. D. Calculation from First-Principles of Golden Rule Rate Constants for Photoinduced Subphthalocyanine/Fullerene Interfacial Charge Transfer and Re-combination in Organic Photovoltaic Cells. *J. Phys. Chem. C* **2014**, *118*, 9780−9789.

(14) Lee, M. H.; Dunietz, B. D.; Geva, E. Donor-to-Donor vs Donor-to-Acceptor Interfacial Charge Transfer States in the Phthalocyanine-Fullerene Organic Photovoltaic System. *J. Phys. Chem. Lett.* **2014**, *5*, 3810−3816.

(15) Manna, A. K.; Balamurugan, D.; Cheung, M. S.; Dunietz, B. D. Unraveling the Mechanism of Photoinduced Charge Transfer in Carotenoid−Porphyrin−C_{60} Molecular Triad. *J. Phys. Chem. Lett.* **2015**, *6*, 1231−1237.

(16) Liang, K. K.; Lin, C.-K.; Chang, H.-C.; Villaeys, A. A.; Hayashi, M.; Lin, S. H. Calculation of the Vibrationally Non-Relaxed Photo-Induced Electron Transfer Rate Constant in DyeSensitized Solar Cells. *Phys. Chem. Chem. Phys.* **2007**, *9*, 853−861.

(17) Baiz, C. R.; Kubarych, K. J. Ultrafast Vibrational Stark-Effect Spectroscopy: Exploring Charge-Transfer Reactions by Directly

Monitoring the Solvation Shell Response. *J. Am. Chem. Soc.* **2010**, *132*, 12784−12785.

(18) Kurpiers, J.; Ferron, T.; Roland, S.; Jakoby, M.; Thiede, T.; Jaiser, F.; Albrecht, S.; Janietz, S.; Collins, B. A.; Howard, I. A.; et al. Probing the Pathways of Free Charge Generation in Organic Bulk Heterojunction Solar Cells. *Nat. Commun.* **2018**, *9*, 2038−2011.

(19) Phillips, H.; Zheng, S.; Hyla, A.; Laine, R.; Goodson, T., III; Geva, E.; Dunietz, B. D. Ab Initio Calculation of the Electronic Absorption of Functionalized Octahedral Silsesquioxanes via Time-Dependent Density Functional Theory with Range-Separated Hybrid Functionals. *J. Phys. Chem. A* **2012**, *116*, 1137−1145.

(20) Beyer, A. N.; Richardson, J. O.; Knowles, P. J.; Rommel, J.; Althorpe, S. C. Quantum Tunneling Rates of Gas-Phase Reactions from On-The-Fly Instanton Calculations. *J. Phys. Chem. Lett.* **2016**, *7*, 4374−4379.

(21) Crespo-Otero, R.; Barbatti, M. Recent Advances and Perspectives on Nonadiabatic Mixed Quantum−Classical Dynamics. *Chem. Rev.* **2017**, *118*, 7026−7068.

(22) Sato, K.; Pradhan, E.; Asahi, R.; Akimov, A. V. Charge Transfer Dynamics at the Boron Subphthalocyanine Chloride/C60 Interface: Non-Adiabatic Dynamics Study with Libra-X. *Phys. Chem. Chem. Phys.* **2018**, *20*, 25275−25294.

(23) Patel, K.; Bittner, E. R. Mixed Quantum Classical Simulations of Charge-Transfer Dynamics in a Model Light-Harvesting Complex I. Charge-Transfer Dynamics. *J. Phys. Chem. B* **2020**, *124*, 2149−2157.

(24) Barbara, P. F.; Meyer, T. J.; Ratner, M. A. Contemporary Issues in Electron Transfer Research. *J. Phys. Chem.* **1996**, *100*, 13148−13168.

(25) Ishizaki, A.; Fleming, G. R. Quantum Coherence in Photosynthetic Light Harvesting. *Annu. Rev. Condens. Matter Phys.* **2012**, *3*, 333−361.

(26) Zhao, Y.; Liang, W. Charge Transfer in Organic Molecules for Solar Cells: Theoretical Perspective. *Chem. Soc. Rev.* **2012**, *41*, 1075−1087.

(27) Brédas, J.-L.; Norton, J. E.; Cornil, J.; Coropceanu, V. Molecular Understanding of Organic Solar Cells: The Challenges. *Acc. Chem. Res.* **2009**, *42*, 1691−1699.

(28) Chen, W.-K.; Fang, W.-H.; Cui, G. Integrating Machine Learning with the Multilayer Energy-Based Fragment Method for Excited States of Large Systems. *J. Phys. Chem. Lett.* **2019**, *10*, 7836−7841.

(29) Marcus, R. A. On the Theory of Oxidation−Reduction Reactions Involving Electron Transfer I. *J. Chem. Phys.* **1956**, *24*, 966−978.

(30) Marcus, R. A. Electrostatic Free Energy and Other Properties of States Having Nonequilibrium Polarization I. *J. Chem. Phys.* **1956**, *24*, 979−989.

(31) Marcus, R. A. Electron Transfer Reactions in Chemistry. Theory and Experiment. *Rev. Mod. Phys.* **1993**, *65*, 599.

(32) Tavernier, H. L.; Kalashnikov, M. M.; Fayer, M. D. Photoinduced Intermolecular Electron Transfer in Complex Liquids: Experiment and Theory. *J. Chem. Phys.* **2000**, *113*, 10191−10201.

(33) Sun, X.; Geva, E. Equilibrium Fermi's Golden Rule Charge Transfer Rate Constants in the Condensed Phase: The Linearized Semiclassical Method vs Classical Marcus Theory. *J. Phys. Chem. A* **2016**, *120*, 2976−2990.

(34) Beratan, D. N. Why Are DNA and Protein Electron Transfer So Different? *Annu. Rev. Phys. Chem.* **2019**, *70*, 71−97.

(35) Balamurugan, D.; Aquino, A. J. A.; de Dios, F.; Flores, L., Jr.; Lischka, H.; Cheung, M. S. Multiscale Simulation of the Ground and Photo-Induced Charge-Separated States of a Molecular Triad in Polar Organic Solvent: Exploring the Conformations, Fluctuations, and Free Energy Landscapes. *J. Phys. Chem. B* **2013**, *117*, 12065−12075.

(36) Starovoytov, O. N.; Zhang, P.; Cieplak, P.; Cheung, M. S. Induced Polarization Restricts the Conformational Distribution of a Light−Harvesting Molecular Triad in the Ground State. *Phys. Chem. Chem. Phys.* **2017**, *19*, 22969−22980.

(37) Coalson, R. D.; Evans, D. G.; Nitzan, A. A Nonequilibrium Golden Rule Formula for Electronic State Populations in Non-adiabatically Coupled Systems. *J. Chem. Phys.* **1994**, *101*, 436−448.

(38) Evans, D. G.; Coalson, R. D. Simulation of electron transfer in polar solvents: Effects of nonequilibrium initial state preparation. *J. Chem. Phys.* **1996**, *104*, 3598−3608.

(39) Izmaylov, A. F.; Mendive-Tapia, D.; Bearpark, M. J.; Robb, M. A.; Tully, J. C.; Frisch, M. J. Nonequilibrium Fermi Golden Rule for Electronic Transitions Through Conical Ontersections. *J. Chem. Phys.* **2011**, *135*, 234106−234115.

(40) Sun, X.; Geva, E. Nonequilibrium Fermi's Golden Rule Charge Transfer Rates via the Linearized Semiclassical Method. *J. Chem. Theory Comput.* **2016**, *12*, 2926−2941.

(41) Sun, X.; Geva, E. Non-Condon Nonequilibrium Fermi's Golden Rule Rates from the Linearized Semiclassical Method. *J. Chem. Phys.* **2016**, *145*, 064109.

(42) Kananenka, A. A.; Sun, X.; Schubert, A.; Dunietz, B. D.; Geva, E. A Comparative Study of Different Methods for Calculating Electronic Transition Rates. *J. Chem. Phys.* **2018**, *148*, 102304.

(43) Sun, X.; Geva, E. Non-Condon Equilibrium Fermi's Golden Rule Electronic Transition Rate Constants via the Linearized Semiclassical Method. *J. Chem. Phys.* **2016**, *144*, 244105.

(44) Sun, X.; Zhang, P.; Lai, Y.; Williams, K. L.; Cheung, M. S.; Dunietz, B. D.; Geva, E. Computational Study of Charge-Transfer Dynamics in the Carotenoid−Porphyrin−C60 Molecular Triad Solvated in Explicit Tetrahydrofuran and Its Spectroscopic Signature. *J. Phys. Chem. C* **2018**, *122*, 11288−11299.

(45) Tong, Z.; Gao, X.; Cheung, M. S.; Dunietz, B. D.; Geva, E.; Sun, X. Charge transfer rate constants for the carotenoid-porphyrin-C60 molecular triad dissolved in tetrahydrofuran: The spin-boson model vs the linearized semiclassical approximation. *J. Chem. Phys.* **2020**, *153*, 044105.

(46) Cho, M.; Silbey, R. J. Nonequilibrium photoinduced electron transfer. *J. Chem. Phys.* **1995**, *103*, 595−606.

(47) Pollak, E.; Plimak, L. Control of thermal photoinduced electron transfer reactions in the activated and activationless regimes. *J. Chem. Phys.* **2001**, *115*, 1867−1874.

(48) Baer, R.; Neuhauser, D. Density Functional Theory with Correct Long-Range Asymptotic Behavior. *Phys. Rev. Lett.* **2005**, *94*, 043002.

(49) Livshits, E.; Baer, R. A Well-Tempered Density Functional Theory of Electrons in Molecules. *Phys. Chem. Chem. Phys.* **2007**, *9*, 2932−2941.

(50) Stein, T.; Eisenberg, H.; Kronik, L.; Baer, R. Fundamental Gaps in Finite Systems from Eigenvalues of a Generalized Kohn-Sham Method. *Phys. Rev. Lett.* **2010**, *105*, 266802.

(51) Voityuk, A. A.; Rösch, N. Fragment Charge Difference Method for Estimating Donor−Acceptor Electronic Coupling: Application to DNA π-Stacks. *J. Chem. Phys.* **2002**, *117*, 5607−5616.

(52) Case, D. A.; Ben-Shalom, I. Y.; Brozell, S. R.; Cerutti, D. S.; Cheatham, T. E., III; Cruzeiro, V. W. D.; Darden, T. A.; Duke, R. E.; Ghoreishi, D.; Gilson, M. K.; et al. *AMBER 2018*; University of California: San Francisco, 2018.

(53) Cornell, W. D.; Cieplak, P.; Bayly, C. I.; Gould, I. R.; Merz, K. M.; Ferguson, D. M.; Spellmeyer, D. C.; Fox, T.; Caldwell, J. W.; Kollman, P. A. A Second Generation Force Field for the Simulation of Proteins, Nucleic Acids, and Organic Molecules. *J. Am. Chem. Soc.* **1995**, *117*, 5179−5197.

(54) Darden, T.; York, D.; Pedersen, L. Particle Mesh Ewald: An Nlog(N) Method for Ewald Sums in Large Systems. *J. Chem. Phys.* **1993**, *98*, 10089−10092.

(55) Ciccotti, G.; Ryckaert, J. P. Molecular Dynamics Simulation of Rigid Molecules. *Comput. Phys. Rep.* **1986**, *4*, 346−392.

(56) Lee, M. H.; Geva, E.; Dunietz, B. D. The Effect of Interfacial Geometry on Charge-Transfer States in the Phthalocyanine/Fullerene Organic Photovoltaic System. *J. Phys. Chem. A* **2016**, *120*, 2970−2975.

(57) Tinnin, J.; Bhandari, S.; Zhang, P.; Aksu, H.; Maiti, B.; Geva, E.; Dunietz, B. D.; Sun, X.; Cheung, M. S. Molecular-Level Exploration of

the Structure-Function Relations Underlying Interfacial Charge Transfer in the Subphthalocyanine/C_{60} Organic Photovoltaic System. *Phys. Rev. Appl.* **2020**, *13*, 054075.

(58) Mandal, A.; Huo, P. Investigating New Reactivities Enabled by Polariton Photochemistry. *J. Phys. Chem. Lett.* **2019**, *10*, 5519−5529.

(59) Renger, T.; Dankl, M.; Klinger, A.; Schlücker, T.; Langhals, H.; Müh, F. Structure-Based Theory of Fluctuation-Induced Energy Transfer in a Molecular Dyad. *J. Phys. Chem. Lett.* **2018**, *9*, 5940−5947.